 doi:10.20944/preprints202104.0388.v1

Article

Experimental Study of Absorbent Hygiene Product devolatilization in a bubbling fluidized bed

Barbara Malsegna [1], Andrea Di Giuliano [1] and Katia Gallucci [1,*]

[1] Department of Industrial and Information Engineering and Economics (DIIIE), University of L'Aquila, Piazzale E. Pontieri 1-loc. Monteluco di Roio, 67100 L'Aquila, Italy; diiie.sac@strutture.univaq.it

* Correspondence: katia.gallucci@univaq.it; Tel.: +39 0862-434213

Abstract: This paper aims to investigate the usage of waste from Absorbent Hygienic Products (AHP) as a fuel for gasification or pyrolysis, two attractive routes to obtain valuable products and dispose of this kind of waste. The study experimentally investigated the devolatilization of coarsely shredded materials from diapers, in a laboratory-scale bubbling fluidized bed made of sand, as a representative preparatory step of above-mentioned thermochemical conversions. Two versions of shredded materials were considered: as-manufactured diapers (AHPam, as a reference), and the cellulosic fraction of sterilized used diapers (AHPus). Results were presented, obtained from physic-chemical characterization of AHPam and AHPus (TGA, CHNS/O, proximate and ultimate analysis, XRF, ICP-AES, SEM-EDS) and their devolatilizations at 500-600-700-800°C, under two different atmospheres (air plus nitrogen, or pure nitrogen as a reference). Generally, temperature had most influenced syngas composition, with better performances under pure nitrogen. At 700-800 °C under pure nitrogen, the highest syngas quality and yield were obtained. For AHPam and AHPus, respectively: (i) H_2 richness equaled 29.5 vol% and 23.7 vol%, while hydrocarbons poorness equaled 14.8 vol% and 7.4 vol% on dry, dilution-free basis; (ii) 53.7 Nl 100 g_{fuel}^{-1} and 46.0 Nl 100 g_{fuel}^{-1} were produced. Overall, AHP emerged as an interesting fuel for thermochemical conversions.

Keywords: absorbent hygiene product; waste; gasification; devolatilization; pyrolysis; fluidized bed; diapers; cellulosic fraction

1. Introduction

The complexity of current global energy issues and the urgency of global warming containment has intensified research efforts regarding renewable and sustainable energy sources [1].

World population is expected to increase up to more than 11 billion people by the end of XXI century, geographically concentrated in the currently least developed regions of the world [2]. This will involve net economic growth in those regions, with attendant growth of world energy demand, and the consequent consumption of resources and waste generation, if the current model of linear economy is kept [3].

In September 2018, the World Bank announced that global waste production was predicted to increase by 70% (referring to 2018) by 2050 [4], unless actions were taken to break the "take-make-waste" paradigm of linear economy. Humankind in 2018 (7.6 billion people) produced two billion tonnes of waste per year; the expected world population growth should therefore be compensated by avoiding the current gross mismanagement of waste [3].

In this framework, the European Union (EU) has promoted thematic strategies regarding waste prevention and recycling, as well as regulations for the transition towards a circular and sustainable economy [5]. In this scenario, several governmental programs have sustained actions to contrast climate change, as recently required by Paris agreement and the subsequent Conferences of the Parties to the United Nations Framework Conventions on Climate Change [6–9]. The European Green Deal represents an important

 doi:10.20944/preprints202104.0388.v1

response to climate change, setting the final goal of EU climate neutrality by 2050; EU aims to couple this goal with a new growth strategy and a just transition towards a modern, competitive and resource efficient socio-economic system [10].

The use of waste as a feedstock is fundamental in a circular economy for applications in energy and biofuel production, since it is one of the pillars of the 2030 Agenda for Sustainable Development and contributes to decarbonization and landfill diversion [11]. Thermochemical conversions may act as an essential part of a sustainable integrated waste management system, as they are suitable routes to produce energy and fuels from waste [12–14]. In the first place, thermal treatment plants can directly convert the chemical energy content of waste in power and process heat [15]. In addition, thermochemical conversions such as pyrolysis and gasification allow obtaining more valuable fuels or chemical products (e.g., by catalytic conversions of syngas [16]), with the advantages of an efficient treatment applicable to different types of solid waste [12–15].

Although biomass utilization in thermochemical processes for energy and chemicals production has been extensively studied in the literature [1,17,18], homologue studies concerning solid waste lead to less unitary conclusions, because of the broader heterogeneity of waste materials. This causes the need of studies dedicated to the behavior of each given class of wastes, in order to develop the related waste-to-energy/fuel/chemicals chain. This necessity has indeed promoted the birth of various projects, such as: "opti-COM", an industrial project aiming to implement fluidized-bed gasification of several solid wastes at industrial scale; "Lig2Liq", a European research project co-funded by the Research Fund for Coal and Steel of European Commission, which investigates co-gasification of lignite with Solid Recovered Fuel (SRF) [13,19]; more than sixty projects funded in the Biomass, Biofuels and Alternative fuel field, by the EU HORIZON2020 program [20].

Absorbent Hygiene Products (AHP) constitute one of those class of wastes, classified as a sanitary waste according to European Waste Catalogue code (EWC, Directive 2000/532/EC). AHP consist of a broad category of products, including diapers for babies, sanitary protection pads, tampons, adult incontinence products and personal care wipes. AHP wastes currently represent about 2-3% of municipal solid waste and up to 15-25% of the residual waste stream in some treatment facilities [21].

Nowadays, wastes from AHP are quite challenging from the sustainability point of view, since they have not been currently recycled but usually disposed of via either landfill or incineration [22]. In literature, some studies reported about the separation of AHP waste into its different material components, which can be then recycled into secondary raw materials with multiple potential uses (e.g. plastic, cellulose fibre plus super absorbent polymers) [23–25].

In view of the implementation of integrated and sustainable management of AHP waste, pyrolysis and gasification may represent a viable process option, because of their versatility concerning fed feedstock and uniformity of product classes (e.g., syngas or liquid hydrocarbons) [26–29]. In other words, AHP waste is a potential feedstock for thermochemical conversion pathways.

In the present work, this option was studied from the experimental point of view. Two different AHP waste materials were investigated: as-manufactured, coarsely shredded diapers, and the cellulosic fraction of sterilized, used diapers. Devolatilizations of samples from those AHP wastes were performed in a laboratory-scale bubbling fluidized bed made of sand, as a representative preparatory step of pyrolysis or gasification, respectively intended as thermochemical conversions in the absence of oxidants or in presence of sub-stoichiometric oxidants (in comparison to combustion) [30]. Physical-chemical characterization of investigated materials were presented and discussed, together with their devolatilization performances, evaluated in terms of syngas yield, carbon conversion, syngas composition and cold gas efficiency. Results were compared, from devolatilizations at different temperatures (from 500 °C to 800 °C), and under fully anoxic or slightly oxidant atmospheres.

Preprints (www.preprints.org) | NOT PEER-REVIEWED | Posted: 14 April 2021 doi:10.20944/preprints202104.0388.v1

These investigations provided novel results concerning the behavior of AHP wastes in thermochemical conversions based on fluidized beds, which could be exploited for both scale-up studies and model validations.

2. Materials and Methods

2.1. Waste materials from AHP for devolatilization tests

Two raw materials were selected in this work: (i) as-manufactured, coarsely shredded diapers (AHPam), which represent an industrial post-production waste (**Figure 1a**); (ii) the cellulosic fraction of sterilized used diapers (AHPus), deriving from a diaper sterilization cycle followed by separation of organic and plastic fractions, which both represent a post-consumer material (**Figure 1b**). AHPam and AHPus are classified according to the EWC code as sanitary waste and are generated by AHP.

(a)

(b)

Figure 1: (a) coarsely shredded diapers (AHPam); (b) cellulosic fraction of sterilized diapers (AHPus).

2.2. Characterization of waste materials from AHP

Several physic-chemical characterization of waste AHP materials were performed.

Proximate and ultimate analyses were determined by means of Thermo-Gravimetric Analysis (TGA), muffle test, oven test and elemental analysis (CHNS/O).

TGA was carried out by the Linesis STA PT100 equipment, to determine volatile matter and fixed carbon fraction. The tests were performed as specified by the standard ASTM D142/02 [31]. Three samples of AHPam and three of AHPus (masses in the range 13.0-27.0 mg) underwent thermal treatments in TGA under pure N_2 or air fluxes. The treatment under pure N_2 (16 Nl h^{-1}) consisted of: (i) 10 °C min^{-1} heating ramp from room temperature to 105 °C and 15 min dwell at 105 °C; (ii) 10 °C min^{-1} heating ramp from 105 °C to 950 °C and a 7 min dwell at 950°C. The treatment under air (16 Nl h^{-1}) consisted of: (i) 10 °C min^{-1} heating ramp from room temperature to 700 °C and 15 min dwell at 700 °C; (ii) 10 °C min^{-1} heating ramp from 700 °C to 950 °C and 10 min dwell at 950 °C. For each kind of treatment, blank tests were carried out and used to correct TGA data from actual samples.

Additional TGA tests were carried out concerning combustion under air flux, in order to evaluate the temperature at which thermal oxidative phenomena could be considered as extinguished. For both AHPam and AHPus, TGA combustion tests were carried out under 10 Nl h^{-1} of air, heating from room temperature up to 950 °C at rates of 5, 10 or 20 °C min^{-1}.

Moisture fractions of AHPam and AHPus were determined by measuring the samples mass variation caused by a drying treatment in oven (model MPIM factory Oven SL), keeping the temperature at 105 °C for 24 h (BSE EN 15414-3:2011 standard [32]).

Muffle tests (LENTON type ECF 12/10 equipment) were carried out to quantify AHPam and AHPus ash fractions, with reference to the ISO18122:2015 & 1016-104.4:1998 standard [33], according to the thermal program: (i) 8°C min^{-1} heating ramp from room temperature up to 500 °C with 1 h dwell at 500 °C; (ii) 8 °C min^{-1} heating ramp from 500 °C up to 815 °C with 2 h dwell at 500 °C.

Preprints (www.preprints.org) | NOT PEER-REVIEWED | Posted: 14 April 2021 doi:10.20944/preprints202104.0388.v1

The elemental analyzer CHNS/O PerkinElmer 2400 Series-II was used to perform the ultimate analysis of AHPam and AHPus, measuring their compositions in terms of carbon (C), hydrogen (H), nitrogen (N), sulfur (S) and oxygen (O) mass percentages on dry basis.

The AHPam and AHPus ashes, obtained from the abovementioned muffle treatment at 815 °C, were analysed by X-Ray Fluorescence (XRF) to determine their semi-quantitative elemental composition. The XRF device was a Spectro Xepos I instrument, with wavelength dispersion method, equipped with a detector that does not allow to detect elements with atomic mass lower than that of magnesium (Mg).

Inductively Coupled Plasma Atomic Emission Spectroscopy analyses (ICP-AES) were carried out with VARIAN 720 ES ICP-AES instrument, in order to detect sodium (Na) in the AHPam material, a key element contained in the super-absorbent polymer of diapers (sodium polyacrylate) [34].

XRF and ICP-AES techniques are of interest, since the presence of Na and other mineral elements (e.g., K, Si, Ca, Na, Mg, Al) can lead to the formation of eutectics [35], which can in turn generate low-melting ashes at the temperatures of the processes investigated in this work; these melting species may be responsible of important process issues, as they can develop agglomerates in fluidized beds or obstructions by recondensation in colder areas [36,37].

2.3. Bed material and fluid-dynamic conditions for devolatilization tests

The bed material used for devolatilization tests was sand; its physical properties of fluid-dynamic interest (range of particle diameter d_p and particle density ρ_p) are summarized in **Table 1**. At experimental conditions of devolatilization tests (see Section 2.4), this sand belong to Group B of generalized Geldart classification [38], for which minimum fluidization velocity coincides with minimum bubbling velocity, i.e., Group B materials cannot provide homogeneous fluidization. From here on, the term "minimum fluidization velocity (u_{mf})" is used to name the beginning of sand fluidization, which is for sure at bubbling regime. Values of u_{mf} (**Table 1**), used as references to set devolatilization experimental conditions in this work (see Section 2.4), were determined according to the method described by Di Giuliano et al. [36].

Table 1. Bed material: physical properties of fluid-dynamic interest and minimum fluidization velocity (u_{mf}) as a function of temperature at devolatilization conditions described in Section 2.4.

Bed material	Sand
d_p (μm)	212-250
ρ_p (kg m^{-3})	2587
T (°C)	**u_{mf} (cm s^{-1})**
500	2.9
600	2.7
700	2.5
800	2.3

2.4. Devolatilization tests: experimental rig and procedure

Devolatilizations tests were performed for both waste materials from AHP, introduced in Section 2.1 (AHPam and AHPus). Each material was investigated at four temperature levels (500, 600, 700, 800 °C) and with two fluidizing agents (pure N_2, or air diluted by N_2 to get 1.3-2.3 vol% of O_2 at the bed inlet). Devolatilizations with pure N_2 may be considered as preparatory experiments for a pyrolysis process, while those with diluted air have the same role regarding gasification.

The laboratory-scale plant for devolatilizations tests is described in detail elsewhere [36]. For the sake of brevity and clarity, only basic information is given here about this experimental rig (**Figure 2**). It included (**Figure 2**) one fluidized bed quartz reactor (5 cm internal diameter), heated by a cylindrical electric furnace, in turn controlled by a thermocouple submerged in the bed. The reactor was fed upward by the fluidizing agent, with

Preprints (www.preprints.org) | NOT PEER-REVIEWED | Posted: 14 April 2021 doi:10.20944/preprints202104.0388.v1

its flow rate set to always develop 1.4 times u_{mf} (**Table 1**) at chosen test conditions. The mass of sand in the reactor was selected in order to obtain 7.5 cm high beds (1.5 times the bed diameter).

Devolatilization products left the reactor from its top with the fluidizing agent, which also serves as a carrier; condensable species were separated by an ice trap and a double-pipe glass condenser at 0 °C. the composition of dry product gases was measured online by an ABB analysis system and a micro gas-chromatograph (μCG) AGILENT 490 (see [36] for further details). The ABB system measured the concentrations of CO, CO_2, CH_4 and H_2 and the overall hydrocarbons content as ppm_v of equivalent C_3H_8. Raw values of equivalent C_3H_8 measured by the ABB system included CH_4 contribution; in this work, the quantity presented as "equivalent C_3H_8" is intended as already reduced by the contribution of CH_4. From here on, "equivalent C_3H_8" means "hydrocarbons with two or more carbon atoms".

Because of the fluffy nature of raw AHP materials (**Figure *1***), prior to devolatilization AHPam and AHPus were compacted in the form of circular tablets by means of a press, then cut in half to obtain individual pieces that could be fed to the reactor (about 0.2-0.4 g per piece).

AHPam and AHPus pieces were fed individually by hand, thanks to a vertical double valve system at the top of the reactor (**Figure 2**, see [36] for further details).Each piece experienced an abrupt temperature variation, from ambient value to the bed one, just in the small duration of piece fall. This fast temperature increase could not be performed by TGA.

For each set "material kind/fluidizing agent/bed temperature", three individual pieces were devolatilized, constituting three repetitions of a given test condition. The thermal decomposition of each piece was carried out until completion, before feeding the following; therefore, the process could be considered as a semi-batch, intrinsically at unsteady state.

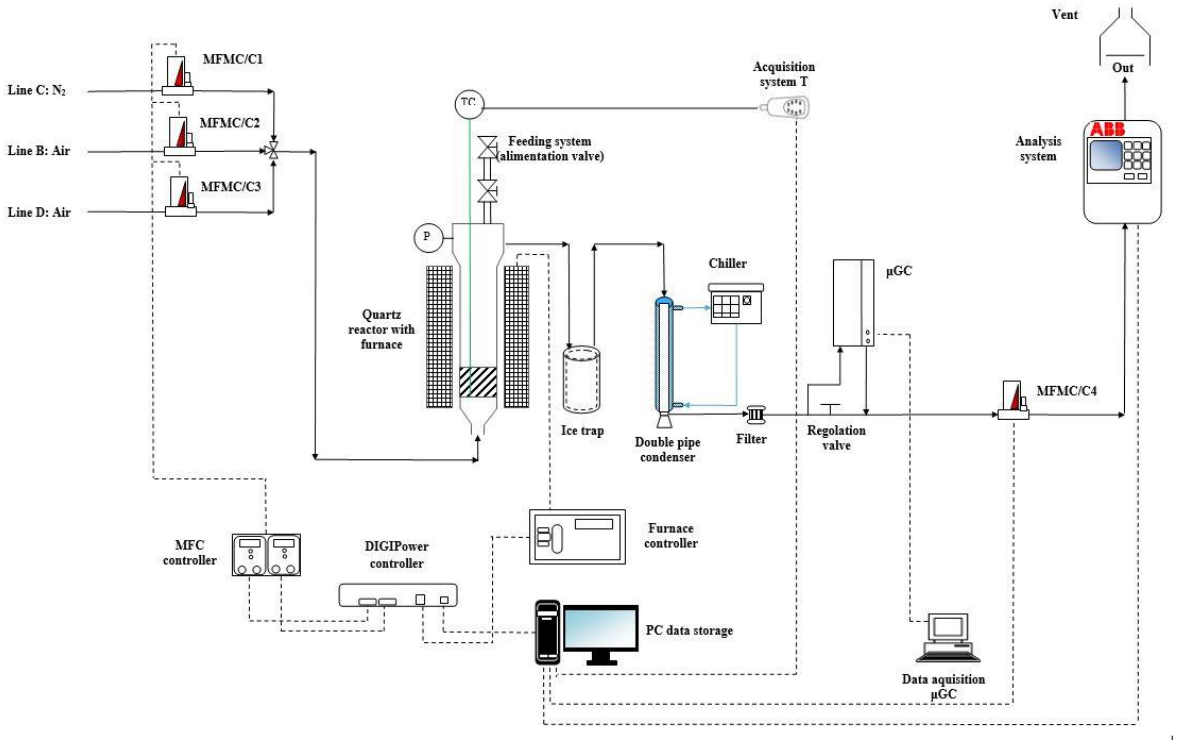

Figure 2: Schematic view of the laboratory-scale experimental apparatus for devolatilization tests

Outlet molar flow rates ($F_{i,out}$, with i = H_2, CO, CO_2, CH_4 and equivalent C_3H_8) as functions of time (t) were obtained from ABB measurements, thanks to the assumption of the N_2 inlet flow rate as the internal standard. With regard to tests involving diluted air, it is reasonable to hypothesize that fed O_2 was mostly converted and, in any case, it

Preprints (www.preprints.org) | NOT PEER-REVIEWED | Posted: 14 April 2021 doi:10.20944/preprints202104.0388.v1

represented a negligible flow rate in comparison to N_2 one; therefore, fed N_2 was always assumed as the internal standard. Once $F_{i,out}$, masses of fuel pieces (m_p) and their compositions (see Section 3.1**Error! Reference source not found.**) were know, mole balances were performed. On the basis of these balances, for each devolatilization, integral-average values ("*av*" superscript in Equations 1, 2, 3) were calculated for the following quantities:

- gas yield (η^{av}, Equation 1);
- percentage of i on dry and dilution free basis (Y^{av}_i, Equation 2);
- carbon conversion (χ^{av}_C, Equation 3, with n_j as the number of C atoms in j);

For quantities defined in Equations 1, 2, 3, averages out of the three repetition were calculated for each set "material kind/fluidizing agent/bed temperature", provided with related standard deviations.

$$\eta^{av} = \frac{\sum_i \int F_{i,out}\, dt}{m_p} \quad with\ i = H_2, CO, CO_2, CH_4\ and\ equivalent\ C_3H_8 \tag{1}$$

$$Y_i^{av} = \frac{\int F_{i,out}\, dt}{\sum_i \int F_{i,out}\, dt} 100 \quad with\ i = H_2, CO, CO_2, CH_4\ and\ equivalent\ C_3H_8 \tag{2}$$

$$\chi_C^{av} = \frac{(12\ g\ mol^{-1}) \times \sum_j \left(n_j \int F_{j,out}\, dt\right)}{m_p \left(\frac{100 - wt\%ar\ of\ moisture}{100}\right)\left(\frac{wt\%db\ of\ C}{100}\right)} 100 \quad with\ j = CO, CO_2, CH_4\ and\ equivalent\ C_3H_8 \tag{3}$$

For each set "material kind/fluidizing agent/bed temperature", cold gas efficiency was calculated as an additional overall evaluation parameter, out of the three repetitions (ξ, Equation 4, with $LHV_{g,i}$ as the Lower Heating Value of gaseous species i in the product gas, LHV_p as Lower Heating Value of the solid fuel).

$$\xi = \frac{\sum_k \left[\left(\sum_i \left(LHV_{g,i} \int F_{i,out} dt\right)\right)_k / m_{p,k}\right]}{3 \cdot LHV_p} \tag{4}$$

$with\ i = H_2, CO, CO_2, CH_4\ and\ equivalent\ C_3H_8\ ;\ k = repetitions\ 1, 2, 3$

Values of LHV in Equation 4 were found in literature for all the syngas components [39][40] and both tested AHP materials [34] (**Table 2**).

Table 2. Calorific value of gas ($LHV_{g,i}$) and sample (LHV_P)

Gas	$LHV_{g,i}$ [MJ kmol^{-1}]	Ref
CO	282.99	[39]
CO_2	0	
H_2	241.83	[39]
CH_4	802.34	[39]
C_3H_8	46.2	[40]
Material	**LHV_P [MJ kg^{-1}]**	
AHPam	23.60	[34]
AHPus	10.36	[34]

2.5. Characterization of the reactor bed after devolatilization tests

Some morphological and topological aspects were observed by microscopy techniques: (i) Scanning Electron Microscopy (SEM) with Zeiss GeminiSEM 500 microscope

Preprints (www.preprints.org) | NOT PEER-REVIEWED | Posted: 14 April 2021 doi:10.20944/preprints202104.0388.v1

equipped with Energy Dispersive X-ray Spectrometry (EDS) for elemental analysis; (ii) observation through a stereomicroscope Leica s8 Apo model.

Results of EDS analyses are mentioned in the discussion of Section 3.3, but only related SEM micrographs are shown. Both microscopy techniques were exploited to study possible agglomeration or sintering phenomena in the fluidized bed, which can interfere with the fluidization quality by increasing the average diameter of the particles, and then affect the performance of thermochemical conversion [39].

This characterization was carried out on the spent fluidized sand at the end of the devolatilization tests (see Section 2.3); the sampling of spent bed was differentiated by zones: coarse agglomerates of the sand bed (**Figure 3**a), top of the sand bed (**Figure 3**b), bottom of the sand bed (**Figure 3**c), and intermediate part of the sand bed (**Figure 3**d).

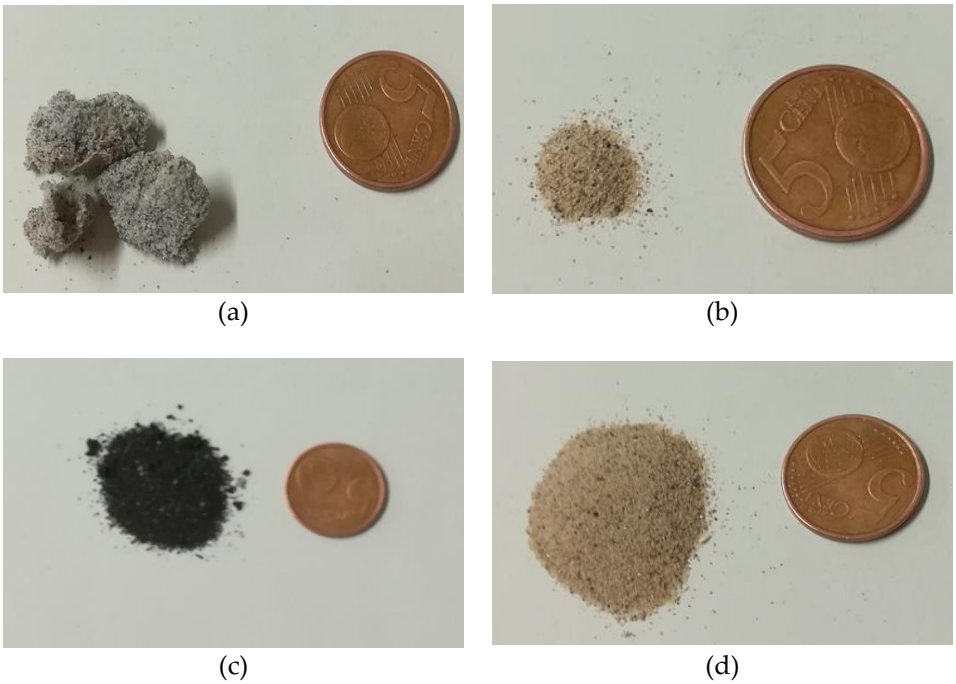

(a) (b) (c) (d)

Figure 3: Sampling of the spent bed after the devolatilization tests: (a) coarse agglomerates of the bed, (b) top of the bed, (c) bottom of the bed, (d) intermediate part of the bed

3. Results

3.1. Results of physic-chemical characterization of AHPam and AHPus

Table 3 shows numerical results of proximate and ultimate analyses of AHPam and AHPus obtained by TGA, oven tests, muffle tests, and CHNS/O analyzer (see Section 2.2),

Table 3 Proximate and ultimate analysis of AHPam and AHPus (ar = as received; db = dry basis)

	wt%ar	
	AHPam	AHPus
Dry weight	94.2	93.4
Moisture	5.8	6.6
Ashes	7.5	10.7.
Volatile matter	82.8	81.5
Fixed carbon	3.9	1.2
	wt%db	
C	65.3	43.5
H	10.3	6.6
N	0.0	0.1

Preprints (www.preprints.org) | NOT PEER-REVIEWED | Posted: 14 April 2021 doi:10.20944/preprints202104.0388.v1

S	1.1	1.8
O[1]	23.3	48.0

Table 4 summarizes the semi-quantitative elemental composition for AHPam and AHPus, measured by XRF (see Section 2.2).

Table 4. Semi-quantitative elemental composition by X-ray fluorescence (XRF) for both ash sample (abs. err. = absolute error)

Element	AHPam		AHPus	
	(wt%)	abs. err. (wt%)	(wt%)	abs. err. (wt%)
Mg	1.007	0.031	< 0.0020	0.0
Al	< 0.0020	0.0	< 0.0020	0.0
Si	0.1016	0.0024	1.272	0.008
P	0.0581	0.001	0.5238	0.0034
S	0.03947	0.00049	4.467	0.005
Cl	0.0079	0.00016	1.425	0.002
K	0.04641	0.00069	2.935	0.003
Ca	11.99	0.01	1.157	0.002
Ti	1.402	0.001	0.08108	0.00029
V	0.05397	0.0006	0.00465	0.00013
Cr	< 0.00010	0.0	0.00796	0.00006
Mn	0.01207	0.00008	0.00906	0.00007
Fe	0.3068	0.0009	0.2159	0.0006

Table 5 summarizes temperatures at which oxidative decomposition phenomena were no longer detectable during TGA combustions, for both AHPam and AHPus.

Table 5 End decomposition temperature measured during TGA combustions in air flux

Heating rates (°C min $^{-1}$)	5	10	20
Temperature of decomposition end for AHPam (°C)	690	660	540
Temperature of decomposition end for AHPus (°C)	530	520	540

3.2. Results of Devolatilization tests

Figure 4 and **Figure 5** show four examples of devolatilizations at 800 °C, one for each combination "fluidizing agent/material kind". As already noted by Di Giuliano et al. [36] for similar experiments on biomass pellets, gaseous products (H_2,CO,CO_2,CH_4, equivalent C_3H_8 hydrocarbons) were released by an unsteady state process, as evidenced by the characteristic asymmetric shape of $F_{i,out}(t)$ peaks. The numerical integration of $F_{i,out}(t)$ curves with respect to time (t) allowed the calculation of integral-average parameters defined by Equations 1, 2, 3 (see Section 2.4); these values were then averaged out of the three repetitions of pellet devolatilizations for each set of condition "material kind/fluidizing agent/bed temperature". In addition, cold gas efficiencies (Equation 4) were calculated on the basis of abovementioned numerical integrations.

Preprints (www.preprints.org) | NOT PEER-REVIEWED | Posted: 14 April 2021 doi:10.20944/preprints202104.0388.v1

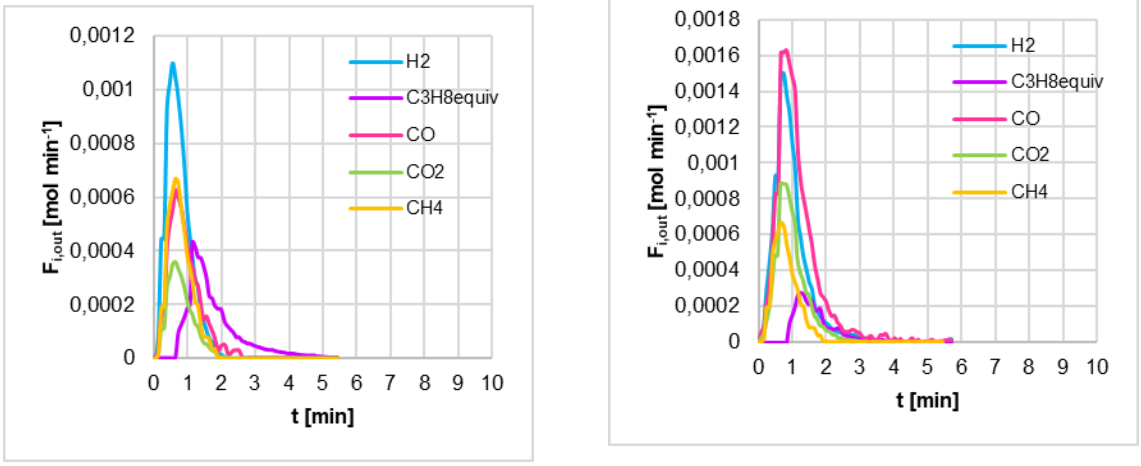

(a) (b)

Figure 4: Example of H_2, CO, CO_2, CH_4 and equivalent C_3H_8 outlet molar flow rates ($F_{i,out}$) as functions of time (t), produced by devolatilizations of (a) AHPam and (b) AHPus, in a fluidized bed, at 800 °C, in nitrogen atmosphere.

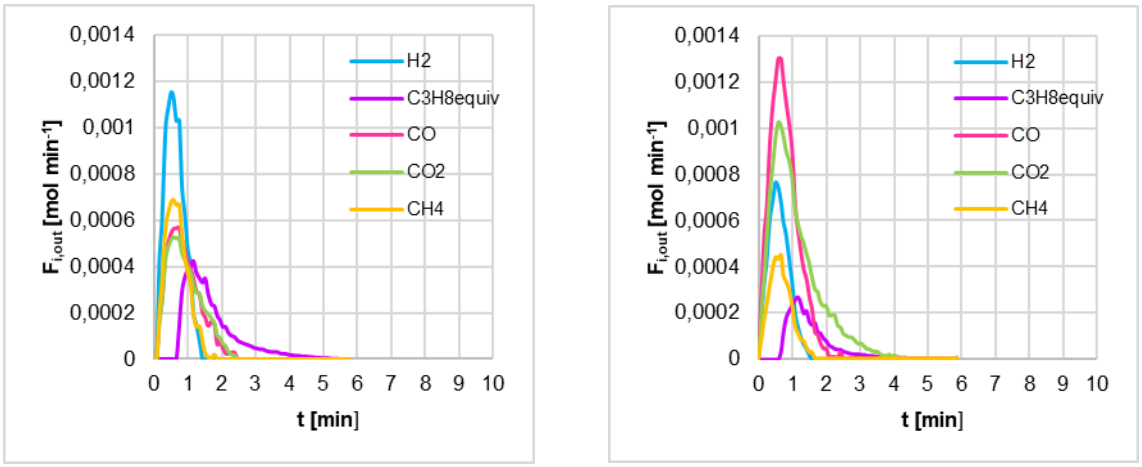

(a) (b)

Figure 5: Example of H_2, CO, CO_2, CH_4 and equivalent C_3H_8 outlet molar flow rates ($F_{i,out}$) as functions of time (t) produced by devolatilizations of (a) AHPam and (b) AHPus, in a fluidized bed, at 800 °C, in nitrogen plus air atmosphere (diluted air)

Bar charts were used to summarize the devolatilization performances of AHP materials in pure nitrogen (**Figure 6**) or diluted air (**Figure 7**), in terms of syngas composition $Y^{av}_{i,out}$ (Equation 2, **Figure 6**a,b, **Figure 7**a,b), carbon conversion χ^{av}_C (Equation 3, **Figure 6**c,d, **Figure 7**c,d), gas yield η^{av} (Equation 1, **Figure 6**e,f, **Figure 7**e,f). In both figures, the left column concerns AHPam, while the right one AHPus.

Colored bars in **Figure 6** and **Figure 7** represent average values out of the three repetitions for each set "material kind/fluidizing agent/bed temperature"; errors bars quantify the related standard deviations.

Numerical data showed in **Figure 6** and **Figure 7** were detailed in the Appendix A of this work.

Preprints (www.preprints.org) | NOT PEER-REVIEWED | Posted: 14 April 2021 doi:10.20944/preprints202104.0388.v1

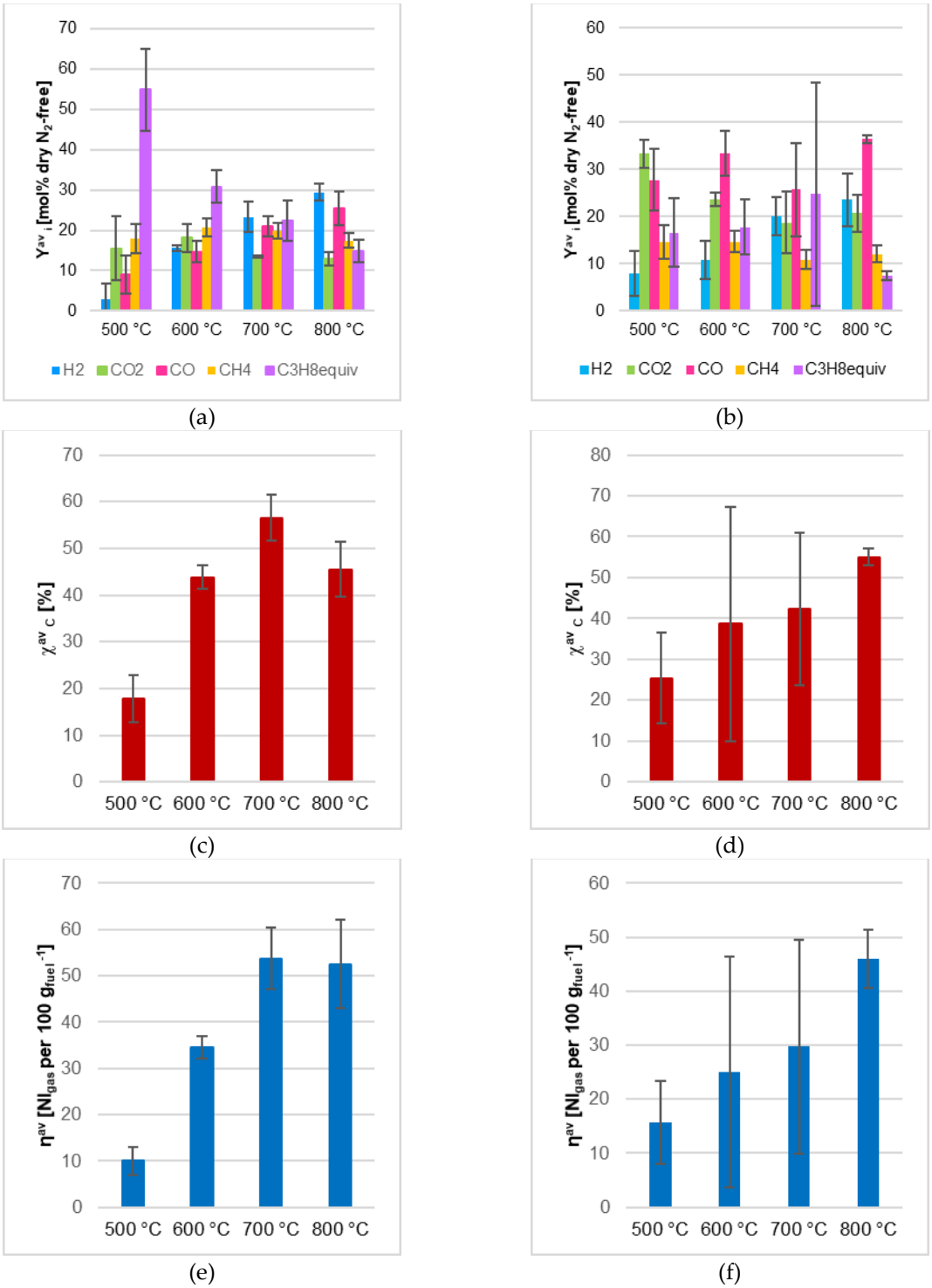

Figure 6: Experimental results of devolatilization tests in nitrogen atmosphere, in a fluidized sand bed, as functions of temperature: integral-average mol% dry, dilution-free ($Y^{av}i^{v}$, Equation 2) of AHPam (a) AHPus (b); integral-average carbon conversion ($\chi^{av}c$, Equation 3) of AHPam (c) AHPus (d); integral-average gas yield (η^{av}, Equation 1) of AHPam (e) AHPus (f); colored bars represent average values out of the three repetitions for each set "material kind/fluidizing agent/bed temperature", errors bars quantify the related standard deviations

Preprints (www.preprints.org) | NOT PEER-REVIEWED | Posted: 14 April 2021 doi:10.20944/preprints202104.0388.v1

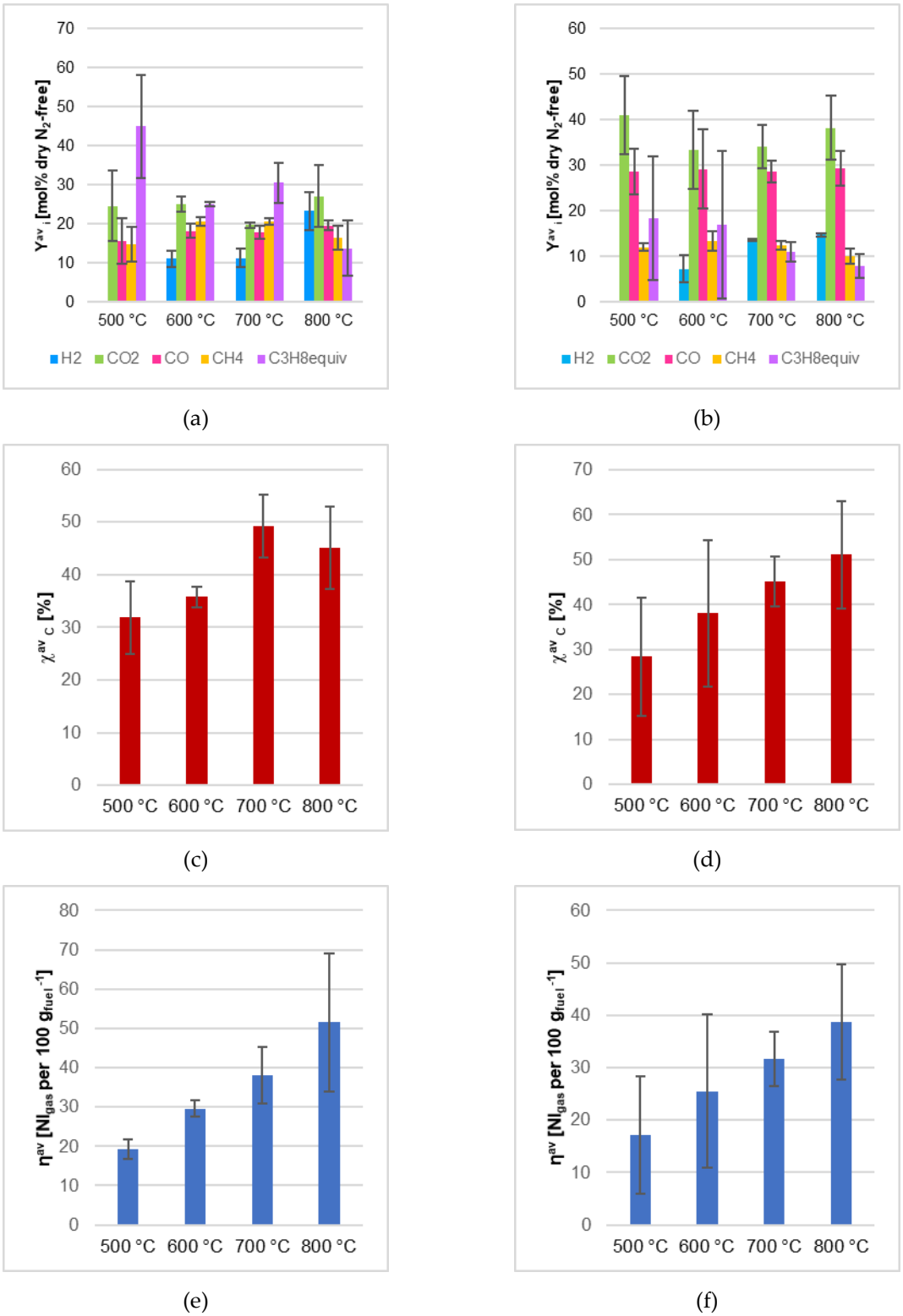

Figure 7: Experimental results of devolatilization tests in nitrogen plus air atmosphere, in a sand bed, as functions of temperature: integral-average mol% dry, dilution-free ($Y^{av}i^{v}$, Equation 2) of AHPam (a) AHPus (b); integral-average carbon conversion ($\chi^{av}{}_C$, Equation 3) of AHPam (c) AHPus (d); integral-average gas yield (η^{av}, Equation 1) of AHPam (e) AHPus (f); colored bars represent average values out of the three repetitions for each set "material kind/fluidizing agent/bed temperature", errors bars quantify the related standard deviations

Preprints (www.preprints.org) | NOT PEER-REVIEWED | Posted: 14 April 2021 doi:10.20944/preprints202104.0388.v1

Table 6 summarized numerical results of cold gas efficiency (ξ, Equation 4) calculated for each set "material kind/fluidizing agent/bed temperature", as described in Section 2.4.

Table 6. Cold gas efficiency (ξ, Equation 4) for each set "material kind/fluidizing agent/bed temperature"

T	Tests with N_2		Tests with N_2 plus air	
	AHPam	AHPus	AHPam	AHPus
(°C)	(%)	(%)	(%)	(%)
500	2.6	16.5	6.8	13.8
600	27.6	27.1	14.3	23.9
700	29.1	32.2	18.6	29.7
800	28.8	51.6	23.8	33.1

3.2. Results spent bed characterizations.

At the end of devolatilization tests, the spent bed material was recovered and sampled by the procedure described in Section 2.5. **Figure 8** shows pictures taken by the stereomicroscope on coarse sand agglomerates (**Figure 3a**). **Figure 9**, **Figure 10**, **Figure 11** and **Figure 12** show SEM micrographs of samples from spent sand bed; more in detail, these picture reveal morphological and topological aspects of coarse agglomerates (**Figure 9**), bed bottom (**Figure 10**), bed intermediate zone (**Figure 11**) and bed top (**Figure 12**).

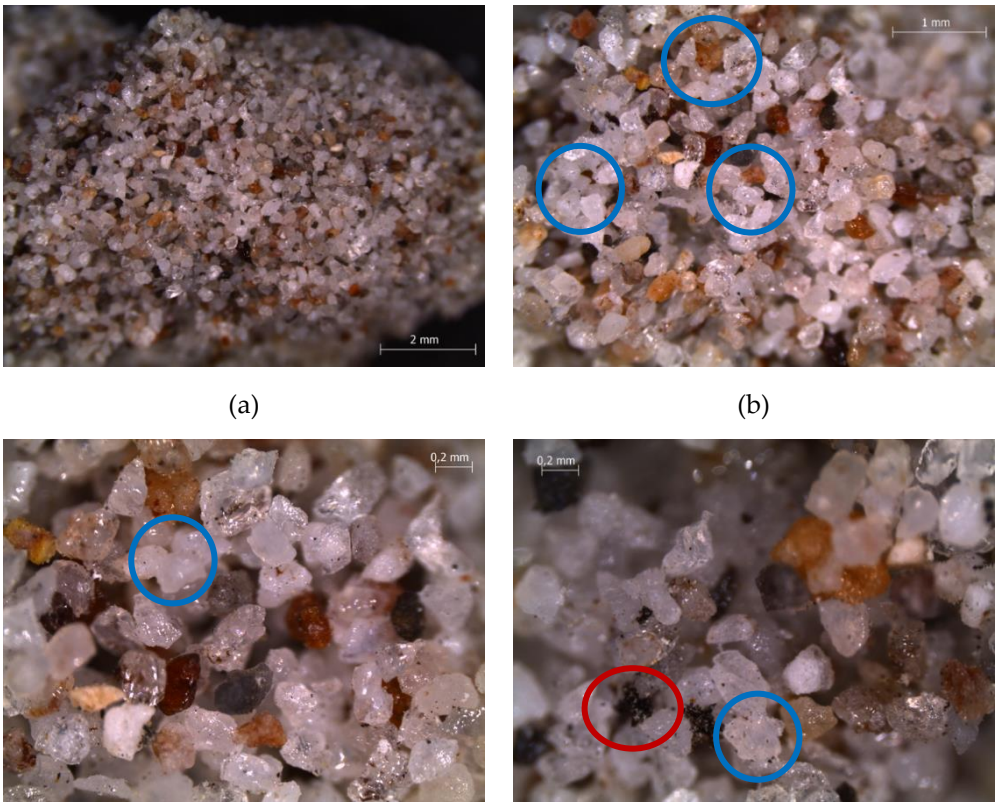

(a) (b)

(c) (d)

Figure 8: Stereo-microscope images of agglomerates of spent sand bed after last test, magnified at: 1x (a); 2x (b); 4x (c); 4x (d)

Preprints (www.preprints.org) | NOT PEER-REVIEWED | Posted: 14 April 2021 doi:10.20944/preprints202104.0388.v1

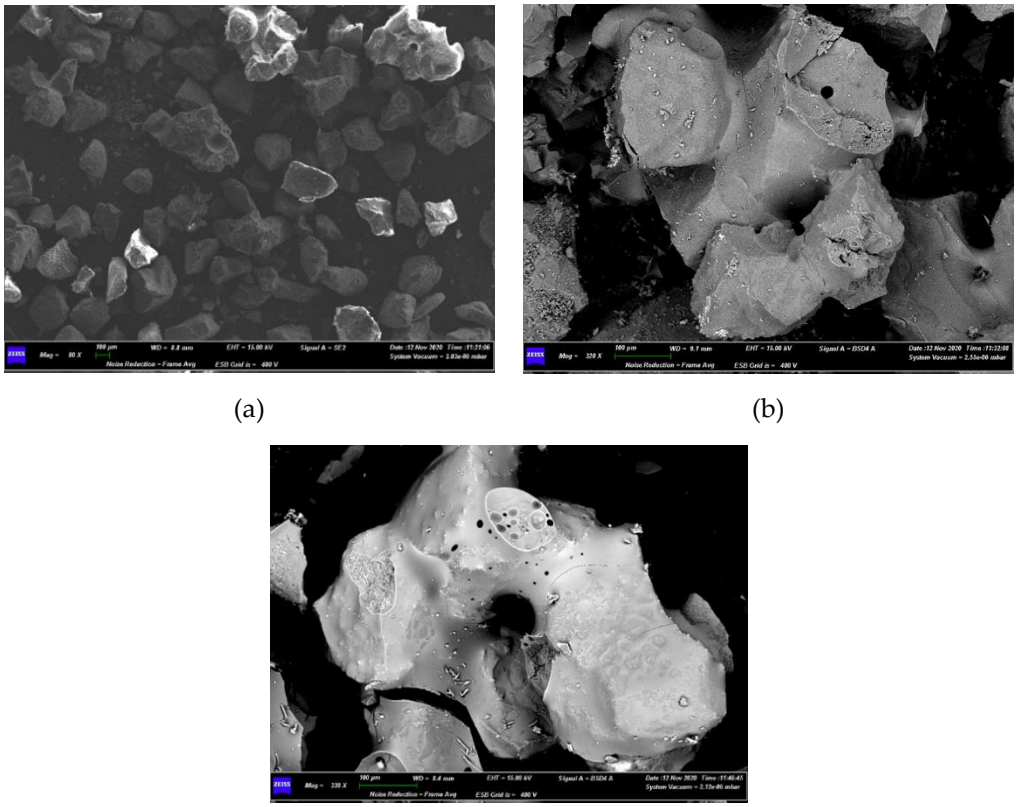

(a) (b)

(c)

Figure 9: SEM micrographs of the coarse agglomerates of spent sand bed after last test, magnified at: 80x (a); 320x (b); 339x (c)

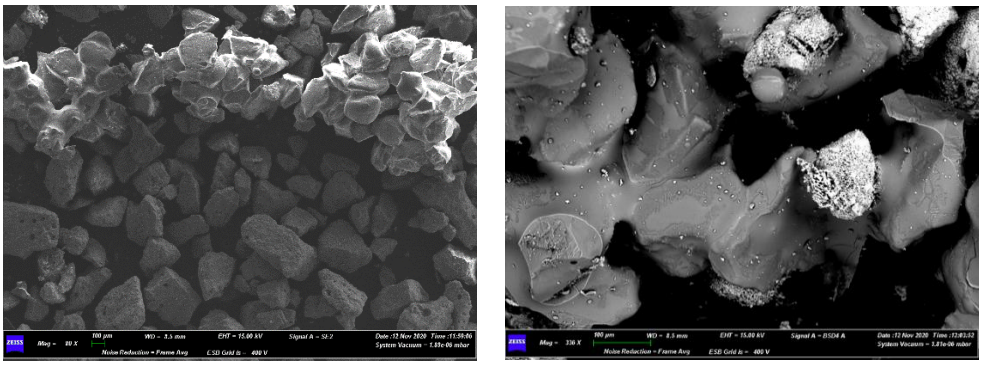

(a) (b)

Figure 10: SEM micrographs of bottom of spent sand bed after last test, magnified at: 80x (a); 336x (b)

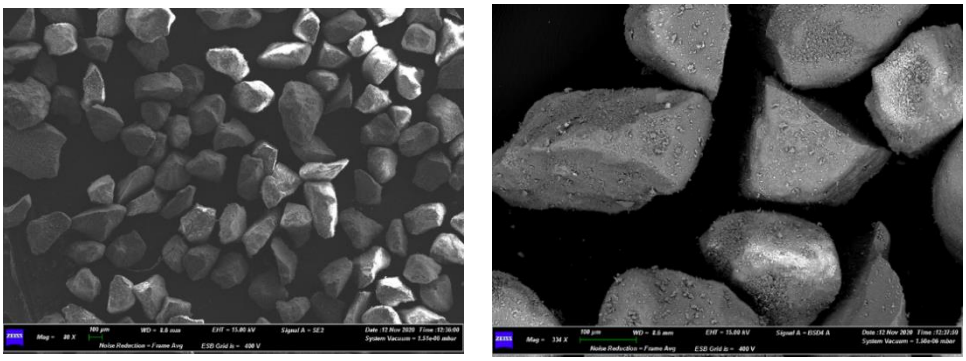

(a)

(b)

Preprints (www.preprints.org) | NOT PEER-REVIEWED | Posted: 14 April 2021 doi:10.20944/preprints202104.0388.v1

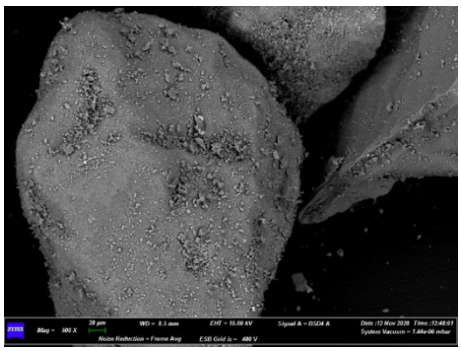

(c)

Figure 11: SEM micrographs of intermediate part of spent sand bed after last test, magnified at: 80x (a); 336x (b); 500x (c)

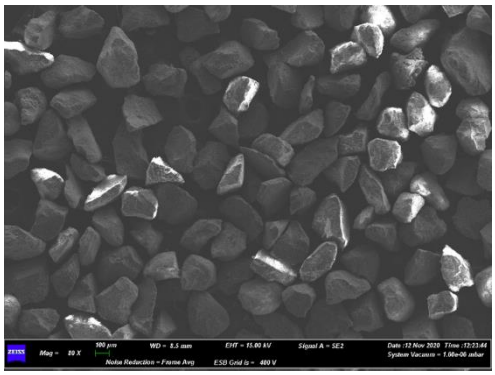

(a)

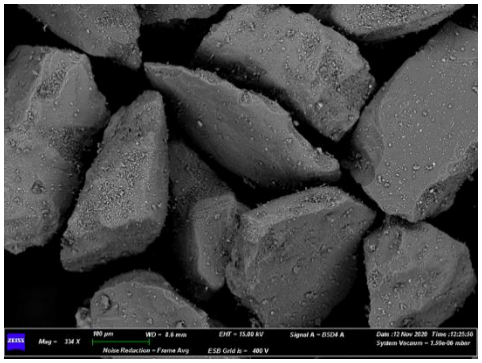

(b)

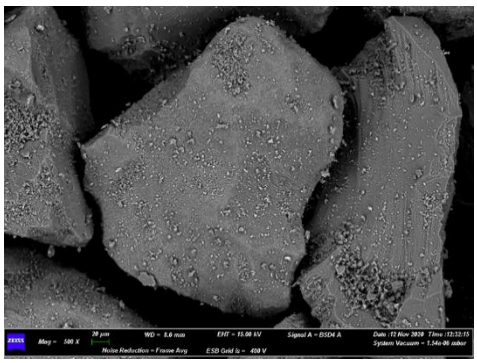

(c)

Figure 12: SEM micrographs of top of spent sand bed after last test, magnified at: 80x (a); 334x (b); 500x (c)

4. Discussion

4.1. Physic-chemical characterizations

Table 3 shows result from proximate and ultimate analyses of AHPam and AHPus. A high volatile content emerged from proximate analyses of both materials (82.8 wt%ar for AHPam and 81.5 wt%ar for AHPus), as well as an important ash fraction (12.5wt% for AHPam and 11.4wt% for AHPus), for instance higher than that of SRF [19]. The high content of volatiles was considered as a positive factor, since the conversion of these species is favored in the thermochemical processes considered in this work [39]. The ultimate analysis highlighted the absence of nitrogen or its presence in traces (0.0 wt%db in AHPam and 0.1wt%db in AHPus, **Table 3**): this could be an interesting feature in an oxyfuel conversion, as it may allow expecting no development of nitrogen-based pollutants.

Preprints (www.preprints.org) | NOT PEER-REVIEWED | Posted: 14 April 2021 doi:10.20944/preprints202104.0388.v1

In general, the ultimate analysis (**Table 3**) for AHPam and AHPus make them appropriate for thermochemical processing.

The semi-quantitative elemental composition, measured by XRF (**Table 4**), identified the main elements in the ashes of AHPam and AHPus. Ashes from AHPam mainly contained Mn, Ca and Ti, while in AHPus ashes there were mainly Si, P, K, Cl, Ca. With regard to S, a not negligible quantity was found in AHPus, higher by one order of magnitude than S in AHPam.

ICP-AES analyses indicated that Na content in AHPam was in the range of 2-3 wt%; it is reasonable to assume a similar Na content in AHPus.

The Na-Si phase diagram [35] shows the formation of an eutectic in the range of temperature of 500-800 °C with 45 wt% of Na in Si). This range of temperature is exactly the one used in devolatilizations of this work. Even though only 2-3 wt% of Na was detected or assumed in AHP-based fuel solids, this value could have become locally hogher, therefore triggering the agglomeration of sand particles. This phenomenon was demonstrated by SEM-EDS analyses of bed samples after devolatilization tests (see Section 3.2, samples of **Figures 8-10**).

4.2. Experimental data of devolatilization tests

With regard to devolatilization tests, it is worth to stress again that they were carried out with two fluidizing agents: pure N_2 or N_2 plus air (i.e., diluted air). Tests with pure N_2 represented a preliminary experimentation which simulated the pyrolysis of AHP waste materials, while those with diluted air did the same for the gasification process [30]. In addition, and more interestingly for the purposes of this work, tests with pure N_2 served as a reference to evaluate effects from the slightly oxidizing atmosphere of experiments with diluted air.

The chosen devolatilization temperatures matched well with results from the combustion tests performed in TGA (**Table 5**), which evidenced that the combustion process ended in a range of temperatures between 500-600 °C. In this regard, from the analysis of these results at 20 °C min^{-1} (the fastest heating rate realized in TGA, **Table 5**), decomposition by combustion extinguished at 540°C for both AHPam and AHPus; considering that devolatilization tests involved a definitively more abrupt temperature increase from room to 500, 600, 700 or 800 °C and that thermal decomposition phenomena tends to overlap as the heating rate is increased, it is reasonable to assume that conditions in the laboratory-scale fluidized bed were sufficient to induce a substantial thermal decomposition of AHP derived fuels.

The results of devolatilizations were presented in Section 3.2. With both fluidizing agents and both AHPam and AHPus, some general effects emerged due to the temperature increase, which were quantified by the parameters defined in Section 2.4.

Integral-average gas yield (η^{av}, Equation 1) for AHPam had maximum values (net of standard deviations) at 700-800 °C in N_2 atmosphere (**Figure 6**e) and at 800 °C in N_2 plus air atmosphere (**Figure 7**e), while η^{av} always increased as the temperature was increased for AHPus with both fluidizing agent, reaching maximum values at 800 °C (**Figure 6**f, **Figure 7**f).

Carbon conversion ($\chi^{av}{}_C$,Equation 3) for AHPam had its maximum value at 700 °C with both fluidizing agents (**Figure 6**c, **Figure 7**c); for AHPus an increasing trend was observed as the temperature was increased, with highest values at 800 °C, even though with important standard deviations at 600 and 700 °C for AHPus in diluted air (**Figure 6**d, **Figure 7**d). These observations highlighted a significant differentiation of behaviors due to the solid fuel nature: with AHPam it is not needed to heat a fluidized bed up to 800 °C to get the maximum $\chi^{av}{}_C$.

As to integral-average gas compositions ($Y^{av}{}_i$, Equation 2, **Figure 6**a,b, **Figure 7**a,b), generally the temperature increase involved an increase of H_2 percentage and a decrease of hydrocarbons fraction (equivalent C_3H_8), with the variations of their two $Y^{av}{}_i$ appearing in reciprocal correlation; it is sensible to hypothesize that hydrogen atoms which were

Preprints (www.preprints.org) | NOT PEER-REVIEWED | Posted: 14 April 2021 doi:10.20944/preprints202104.0388.v1

converted in gaseous H_2 came from the cellulosic and plastic matrix of the AHP materials [34].

Differences emerged concerning the formation of gaseous hydrocarbons, when comparing the gas developed from the two materials: under both atmospheres, the decomposition of AHPam produced a syngas with higher equivalent C_3H_8 fraction (**Figure 6**a vs. **Figure 6**b, **Figure 7**a vs. **Figure 7**b). This difference was exalted at 500 °C, the lowest investigated temperature: under N_2, $Y^{av}_{C3H8equiv}$ was 54.8 vol% for AHPam (**Figure 6**a) and 16.5 vol% for AHPus (**Figure 6**b) on dry and dilution-free basis; the same trends and orders of magnitude were observed in the N_2 plus air case (**Figure 7**a vs. **Figure 7**b). This aspect could be correlated to the composition of the material, as the AHPam contained higher carbon and hydrogen fractions than those of AHPus (elemental analyses, **Table 3**). This effect due to AHP materials decreased as the temperature was increased.

A deeper qualitative insight about hydrocarbons nature came from μCG analyses. Peaks with retention times compatible to those of ethylene/acetylene and propene were often detected at all tested temperatures, while benzene was occasionally found in syngas from tests at 800 °C under diluted air. In any case – as evidenced by Di Giuliano et al. for similar tests on the same rig of this work – those μGC analyses are only an optional means to identify some of the hydrocarbons quantified by the ABB system as "equivalent C_3H_8"; it must be taken into account that the sampling was manually started and occurred on a flow produced by an unsteady process [36].

As to oxidized carbon in gases (CO and CO_2), it is reasonable to assume that oxygen could come only from the solid phases in tests under pure N_2, while fed O_2 acted as an additional source in tests with N_2 plus air. This assumption found confirmation in experimental results: for both materials and all temperatures, devolatilizations in diluted air produced syngas with higher fractions of CO and CO_2 (**Figure 7**a,b), in comparison with devolatilizations under pure N_2 (**Figure 6**a,b). On the other hand, in both atmospheres, AHPus had higher fractions of CO and CO_2 (**Figure 6**b, **Figure 7**b) than those of AHPam (**Figure 6**a, **Figure 7**a), in agreement with oxygen content in solid fuels (**Table 3**). The non-linear behavior of CO_2 concentration with respect to temperature could be ascribed to the network of exothermic and endothermic reactions and the competitive trend of their thermodynamic and kinetic peculiarities.

Numerical data represented in **Figure 6** and **Figure 7** were reported in the Appendix A of this work (**Table A1** and **Table A2**) and sometimes important standard deviation were observed. This variability was ascribed to: (i) the macroscopic inhomogeneity of the AHP materials, which made difficult to obtain solid pressed tablets representative of the average composition of each whole bulk inventory; (ii) the low density of the analyzed materials together with allowed dimensions of pressed tablets, which involved small masses of fed fuel per each devolatilization test, implying a more significant relative weight of inherent experimental errors on determined quantities.

The cold gas efficiency (ξ, Equation 4, **Table 6**) was used an overall parameter to better evaluate the experimental devolatilization performances. Results in **Table 6** confirmed that the temperature increase produced positive effects, as it made the ξ grow for both materials and both atmospheres in the range 500-800 °C. At a given temperature, AHPus devolatilizations under both atmospheres resulted into higher ξ values than those related to AHPam (with the minor exception for pure N_2 at 600 °C, **Table 6**). The highest ξ occurred indeed for AHPus, at 800°C: 56.5% in N_2 atmosphere and 33.1 % in N_2 plus air atmosphere, respectively (**Table 6**). This evidence is corroborated by the higher volatiles content in AHPus samples (**Table 3**). These results are in further agreement with the detected improvements of the composition of the produced gas (**Figure 6**a,b, **Figure 7**a,b), i.e., an increase in gaseous compounds with a higher calorific value (H_2, CO and CH_4) as the temperature was increased, with the concomitant increase of gas yield η^{av}. This is a sign that the endothermic processes of devolatilization are favored and the light hydrocarbon compounds, collectively reported as equivalent C_3H_{8e}, were widely decomposed at 800°C.

Preprints (www.preprints.org) | NOT PEER-REVIEWED | Posted: 14 April 2021 doi:10.20944/preprints202104.0388.v1

Overall, among all tested conditions, the range 700-800 °C appears as the best for thermal decomposition of both AHP materials, with better performances in terms of cold gas efficiencies achieved with AHPus at 800 °C.

As a side note, the experimenters of this work would like to underline that important and progressive deposition of allegedly carbonaceous species occurred on the reactor walls and inside downstream pipelines. This made impossible and unrealistic to close carbon balances; as a first approximation, it can be assumed that the share (100 - χ^{av}_C) is attributable to these deposits. This is also a significative issue which must be considered in possible scaled-up processes of AHP waste thermochemical conversions.

4.3. Characterization of bed reactor after tests

The SEM-EDS and stereoscopic microscope analyses allowed deepening the insight about agglomeration of ashes and bed particles, during the devolatilization tests (see Section 2.5).

Figure 8 shows pictures taken by the stereomicroscope on coarse sand agglomerates, shown at 1:1 scale in **Figure 3**a. **Figure 8**a is an overall view of bed particles after the whole devolatilization campaign under N_2 and air atmosphere: many sand particles in the diameter range of 212-250 μm (**Table 1**) appeared as stuck in a very compact block, i.e., agglomerated into coarse groups in the order of 1-2 cm. This phenomenon could negatively affect the fluidization quality of the bed. Magnifications of stereomicroscope pictures (**Figure 8**b,c,d) evidenced the occurrence of Si particles fusion (blue circles) and carbon deposition (red circle).

Figure 9, **Figure 10**, **Figure 11** and **Figure 12** show SEM micrographs of the spent sand bed after last test; more in detail, these picture revealed morphological and topological aspects of coarse agglomerates (**Figure 9**), bed bottom (**Figure 10**), bed intermediate zone (**Figure 11**) and bed top (**Figure 12)**.

Figure 9a shows irregularly shaped particles (dark gray) and some agglomerates (light grey, top right). Those agglomerates were detailed by **Figure 9**b,c: smooth bridges and jagged areas characterized by crusts and holes appeared, together with melted covers which adhered to the original grains. EDS microanalyses highlighted the presence of Si as the main constituent of those bridges, with a lower amount of Na and traces of other elements such as Al, Mg, K and Fe, documented as possible causes of sintering phenomena [41].

In its upper part, **Figure 10**a shows a relatively huge chain of agglomerates, quite evident by contrast with the smaller, well segregated particles below. **Figure 10**b evidences the presence of the same kind of smooth bridges already found in **Figure 9**b,c and areas covered by melted layers (brighter zone in **Figure 10**b), mainly containing Si, Na and traces of K, Al and Ca, according to EDS analyses. In addition, the lightest zone in **Figure 10**b consisted of a porous structure with Ca as its mains constituent.

Intermediate (**Figure 11**) and top (**Figure 12**) zones of the bed revealed a very similar morphology, also at the single particle level, as can be seen by magnified micrographs in **Figure 11**c and **Figure 12**c. A superficial deposition of spread fine particles was observed (**Figure 11**b,c and **Figure 12**b,c.), but no sintering occurred on the whole. SEM-EDS results confirmed that the fine particles were made up of Si and traces of Al, Mg. Na, K and Ca.

Overall, the following observations could be inferred from the microscopic characterization:

1. *a priori*, it was expected to find a greater number of melted particles/agglomerates in the upper part of the bed, because it is the zone of the first contact between falling AHP materials and of its free surface; however, the exact opposite happened and the smaller particles had moved to the top of the bed, while the larger ones, allegedly formed on the top, were found on the bottom. This is a proof of the good mixing within the fluidized bed;
2. agglomerations did not diffusely involve the whole bed inventory. This suggests that only where the bed has experienced locally high Na concentrations, the eutectic

 doi:10.20944/preprints202104.0388.v1

formed [35], even though the quantity of Na in the fed fuel was low (2-3 wt%) compared to Na eutectic concentration in Si (45 wt%) [35].

5. Conclusions

This work dealt with devolatilizations of two kinds of waste generated from Absorbent Hygiene Product (AHP): shredded scarp of as-manufactured diapers (AHPam) and shredded cellulosic fraction of used and sterilized diapers (AHPus). Tests were carried out in a laboratory-scale bubbling fluidized bed made of sand, at temperatures between 500 °C and 800 °C, under inert and mildly oxidizing atmospheres. This experimental campaign served as a preparatory step for possible scaling-up of thermochemical conversion processes with AHP wastes as the solid fuel feedstock.

Devolatilization performances were evaluated in terms of gas yield, carbon conversion and cold gas efficiency.

Temperature appeared as the most influent variable, followed by the oxygen content in the fluidization agent and the kind of solid fuel. Devolatilization tests performed at 700 and 800 °C, using pure nitrogen as the fluidizing agent, allowed obtaining the highest values of gas yield (53.7 Nl 100 g_{fuel}^{-1} for AHPam at 700 °C; 46.0 Nl 100 $g_{fuel}^{-1}$for AHPus at 800 °C), carbon conversion (56.5% for AHPam at 700 °C; 55.0% for AHPus at 800 °C), cold gas efficiency (28.8% for AHPam, 51.6% for AHPus both at 800 °C).

The oxidative atmosphere determined poorer performances in terms of cold gas efficiency, sensibly because of the more pronounced oxidation of gaseous products. According to the same parameter, AHPus appeared as the more interesting fuel feedstock.

Some agglomeration and sintering of the bed particles occurred, ascribed to low-melting elements in the fuel ashes, such as Na, Ca, Si and K, by means of SEM-EDS analyses. Nevertheless, this phenomenon did not spread within the whole bed inventory.

Important depositions of allegedly carbonaceous species were noted inside the reactor and on internal walls of downstream pipelines.

The presented experimental investigation provided results and useful information concerning the behavior of AHP wastes in thermochemical conversions occurring in fluidized beds. Technical issues, such as sand particles agglomeration and dirt depositions, were documented in view of possible scale-up of thermochemical conversion processes of AHP wastes. In addition, devolatilization experimental data were made available for possible model validations in further studies.

Overall, AHP wastes appeared as an interesting feedstock for thermochemical processes, especially if aimed at power/heat production.

Author Contributions: Conceptualization, K.G. and A.D.G.; methodology, K.G. and A.D.G.; softwareA.D.G. and B.M.; validation, K.G. and A.D.G.; formal analysis, K.G. and A.D.G.; investigation, K.G., A.D.G. and B.M.; resources, K.G.; data curation, K.G., A.D.G. and B.M.; writing—original draft preparation, B.M.; writing—review and editing, K.G., A.D.G. and B.M.; visualization, K.G., A.D.G. and B.M.; supervision, K.G.; project administration, K.G.; funding acquisition, K.G. All authors have read and agreed to the published version of the manuscript.

Funding: This research was funded by the by ALMACIS s.r.l.

Acknowledgments: The provision of AHP materials by ALMACIS s.r.l.) is acknowledged. The authors warmly thank Giampaolo Antonelli for his technical support, and Fabiola Ferrante for XRF and CHNS/O analyses and managing.

Conflicts of Interest: The authors declare no conflict of interest. The funders had no role in the design of the study; in the collection, analyses, or interpretation of data; in the writing of the manuscript, or in the decision to publish the results.

Preprints (www.preprints.org) | NOT PEER-REVIEWED | Posted: 14 April 2021 doi:10.20944/preprints202104.0388.v1

Appendix A

This appendix summarizes the numerical results discussed in this manuscript. **Table A1** and **Table A2** show the experimental data of devolatilization tests, discussed in the main text and reported as bar charts in **Figure 6** and **Figure 7**;

Table A1. Experimental results of devolatilization tests in nitrogen atmosphere, as functions of temperature (av3: average of results from the three individual pellets; sd3: standard deviation of results from the three in dividual pellets)

Sample	η^{av} (Nl 100 g_{fuel}^{-1})		$\chi^{av}C$ (%)		Y^{av}_{H2} (mol% dry N_2-free)		$Y^{av}_{C3H8equiv}$ (mol% dry N_2-free)		Y^{av}_{CO} (mol% dry N_2-free)		Y^{av}_{CO2} (mol% dry N_2-free)		Y^{av}_{CH4} (mol% dryN_2-free)	
	av3	**sd3**	**av3**	**sd3**	**av3**	**sd3**	**av3**	**sd3**	**av3**	**sd3**	**av3**	**sd3**	**av3**	**sd3**
						500 °C								
AHPam	10.0	3.11	17.8	5.1	2.80	3.90	54.8	10.2	9.00	4.62	15.5	7.91	17.8	3.63
AHPus	15.8	7.67	25.4	11.1	7.90	4.80	16.5	7.26	27.8	6.50	33.3	3.00	14.5	9.96
						600 °C								
AHPam	34.5	2.43	43.8	2.5	15.6	0.63	30.8	3.96	14.7	2.71	18.1	3.50	20.8	2.24
AHPus	25.0	21.4	38.6	28.7	10.7	4.07	17.7	5.86	33.4	4.66	23.5	1.40	14.7	0.38
						700 °C								
AHPam	53.7	6.66	56.5	4.9	23.3	3.72	22.5	5.03	21.0	2.55	13.5	0.38	19.8	2.02
AHPus	29.8	19.8	42.2	18.7	20.1	4.07	24.7	23.8	25.7	9.79	18.7	6.62	10.8	4.00
						800 °C								
AHPam	52.5	9.51	45.5	5.8	29.5	2.05	14.8	2.80	25.4	4.04	12.9	1.74	17.5	1.73
AHPus	46.0	5.40	55.0	2.1	23.5	5.53	7.40	0.98	36.4	0.89	20.7	3.95	12.0	1.36

Table A2. Experimental results of devolatilization tests in nitrogen plus air atmosphere, as functions of temperature (av3: average of results from the three individual pellets; sd3: standard deviation of results from the three individual pellets)

Sample	η^{av} (Nl 100 g_{fuel}^{-1})		$\chi^{av}C$ (%)		Y^{av}_{H2} (mol% dry N_2-free)		$Y^{av}_{C3H8equiv}$ (mol% dry N_2-free)		Y^{av}_{CO} (mol% dry N_2-free)		Y^{av}_{CO2} (mol% dry N_2-free)		Y^{av}_{CH4} (mol% dry N_2-free)	
	av3	**sd3**	**av3**	**sd3**	**av3**	**sd3**	**av3**	**sd3**	**av3**	**sd3**	**av3**	**sd3**	**av3**	**sd3**
						500 °C								
AHPam	19.2	2.53	31.9	6.9	0.00	0.00	45.0	13.3	15.7	5.90	24.6	9.00	14.8	4.40
AHPus	17.2	11.2	28.4	13.2	0.00	0.00	18.4	13.6	28.6	5.00	41.0	8.50	12.0	0.80
						600 °C								
AHPam	29.6	2.14	35.7	2.00	11.1	2.1	25.0	0.60	18.2	1.90	25.0	2.10	20.6	1.20
AHPus	25.5	14.6	38.0	16.3	7.3	3.3	16.9	16.2	29.1	8.70	33.4	8.60	13.3	2.10
						700 °C								
AHPam	38.0	7.11	49.1	6.00	11.3	2.30	30.5	5.03	17.9	1.70	19.7	0.60	30.5	0.80
AHPus	31.6	5.14	45.1	5.50	13.6	0.30	11.1	2.20	28.6	2.50	34.2	4.80	11.1	1.00
						800 °C								
AHPam	51.5	17.6	45.1	7.90	23.3	5.00	13.8	7.10	19.6	1.20	27.0	7.90	16.3	3.10

AHPus	38.7	10.9	51.1	11.8	14.7	0.40	7.80	2.60	29.3	3.80	38.2	7.10	10.0	1.70

References

1. Perea-Moreno, M.A.; Samerón-Manzano, E.; Perea-Moreno, A.J. Biomass as renewable energy: Worldwide research trends. *Sustain.* **2019**, *11*, doi:10.3390/su11030863.
2. Bongaarts, J. Development: Slow down population growth. *Nature* **2016**, *530*, 409–412, doi:10.1038/530409a.
3. Ellen MacArthur Foundation Circular Economy - UK, USA, Europe, Asia & South America - The Ellen MacArthur Foundation Available online: https://www.ellenmacarthurfoundation.org/.
4. The World Bank What a Waste: An Updated Look into the Future of Solid Waste Management Available online: https://www.worldbank.org/en/news/immersive-story/2018/09/20/what-a-waste-an-updated-look-into-the-future-of-solid-waste-management.
5. EC European Commission – Environment – Circular Economy Strategy Available online: http://ec.europa.eu/environment/circular-economy/index_en.htm.
6. Obama, B. The irreversible momentum of clean energy: Private-sector efforts help drive decoupling of emissions and economic growth. *Science (80-.).* **2017**, doi:10.1126/science.aam6284.
7. Marris, E. Why young climate activists have captured the world's attention. *Nature* **2019**, doi:10.1038/d41586-019-02696-0.
8. United Nations Climate Change The Paris Agreement | UNFCCC Available online: https://unfccc.int/process-and-meetings/the-paris-agreement/the-paris-agreement.
9. COP 24 | UNFCCC Available online: https://unfccc.int/process-and-meetings/conferences/past-conferences/katowice-climate-change-conference-december-2018/sessions-of-negotiating-bodies/cop-24.
10. A European Green Deal | European Commission Available online: https://ec.europa.eu/info/strategy/priorities-2019-2024/european-green-deal_en (accessed on Jan 3, 2021).
11. Johnston, R.B. Arsenic and the 2030 Agenda for sustainable development. *Arsen. Res. Glob. Sustain. - Proc. 6th Int. Congr. Arsen. Environ. AS 2016* **2016**, 12–14, doi:10.1201/b20466-7.
12. Arena, U. Process and technological aspects of municipal solid waste gasification. A review. *Waste Manag.* **2012**, *32*, 625–639, doi:10.1016/j.wasman.2011.09.025.
13. Lombardi, L.; Carnevale, E.; Corti, A. A review of technologies and performances of thermal treatment systems for energy recovery from waste. *Waste Manag.* **2015**, *37*, 26–44, doi:10.1016/j.wasman.2014.11.010.
14. Materazzi, M.; Foscolo, P.U. The role of waste and renewable gas to decarbonize the energy sector. In *Substitute Natural Gas from Waste: Technical Assessment and Industrial Applications of Biochemical and Thermochemical Processes*; 2019 ISBN 9780128155547.
15. Lig2Liq – Cost Effective Conversion of Lignite and Waste to Liquid Fuels Available online: https://www.lig2liq.eu/ (accessed on Jan 3, 2021).
16. Weber, G.; Di Giuliano, A.; Rauch, R.; Hofbauer, H. Developing a simulation model for a mixed alcohol synthesis reactor and validation of experimental data in IPSEpro. *Fuel Process. Technol.* **2016**, doi:10.1016/j.fuproc.2015.05.024.
17. Rapagnà, S.; Gallucci, K.; Foscolo, P.U. Olivine, dolomite and ceramic filters in one vessel to produce clean gas from biomass. *Waste Manag.* **2018**, *71*, 792–800, doi:10.1016/j.wasman.2017.07.038.
18. Molino, A.; Chianese, S.; Musmarra, D. Biomass gasification technology: The state of the art overview. *J. Energy Chem.* 2016, *25*, 10–25.
19. Savuto, E.; Di Carlo, A.; Gallucci, K.; Di Giuliano, A.; Rapagnà, S. Steam gasification of lignite and solid recovered fuel (SRF) in a bench scale fluidized bed gasifier. *Waste Manag.* **2020**, *114*, 341–350, doi:10.1016/j.wasman.2020.07.016.
20. European Comission Innovation and Networks Executive Agency Available online: https://ec.europa.eu/inea/en/connecting-europe-facility/cef-transport/projects-by-country/multi-country/2014-eu-tm-0196-s.

21. Treatment of absorbent hygiene products for improved recycling of materials | Green Best Practice Community Available online: https://greenbestpractice.jrc.ec.europa.eu/node/131#bemp_general_title_id.
22. Waldheim, L. *Gasification of waste for energy carriers - A review*; 2018; https://www.etipbioenergy.eu/databases/reports/353-gasification-of-waste-for-energy-carriers-a-review
23. *Deliverable number 1.7 – Blueprint for the replication of the AHP pretreatment technol*; Establishing a Multi-purpose Biorefinery for the Recycling of the organic content of AHP waste in Circular Economy Domain Grant Agreement No.: 745746,online https://www.embraced.eu/repository/EMBRACED_D1.7_Blueprint_DEF.pdf
24. Mendoza, J.M.F.; D'Aponte, F.; Gualtieri, D.; Azapagic, A. Disposable baby diapers: Life cycle costs, eco-efficiency and circular economy. *J. Clean. Prod.* **2019**, *211*, 455–467, doi:10.1016/j.jclepro.2018.11.146.
25. Kashyap, P.; Ko Win, T.; Visvanathan, C. Absorbent Hygiene Products-An emerging urban waste management issue. Conference Proceedings - *Asia-Pacific Conference on Biotechnology for Waste Conversion* 2016, Hong Kong SAR, P.R. China, 5-8 December 2016
26. Arena, U.; Ardolino, F.; Gregorio, F.D.I. Sustainability of an Integrated Recycling Process of Absorbent Hygiene Products. *15th Int. Waste Manag. Landfill Symp.* **2015**.
27. Gerina-Ancane, A.; Eiduka, A. Research and analysis of Absorbent Hygiene Product (AHP) recycling. In Proceedings of the Engineering for Rural Development; 2016; Vol. 2016-Janua, pp. 904–910.
28. Khanyile, A.; Caws, G.C.; Nkomo, S.L.; Mkhize, N.M. Characterisation study of various disposable diaper brands. *Sustain.* **2020**, *12*, 1–18, doi:10.3390/su122410437.
29. Khoo, S.C.; Phang, X.Y.; Ng, C.M.; Lim, K.L.; Lam, S.S.; Ma, N.L. Recent technologies for treatment and recycling of used disposable baby diapers. *Process Saf. Environ. Prot.* **2019**, *123*, 116–129, doi:10.1016/j.psep.2018.12.016.
30. Roddy, D.J.; Manson-Whitton, C. *Biomass gasification and pyrolysis*; 2012; Vol. 5; ISBN 9780080878737.
31. Bassano, C.; Deiana, P.; Ricci, G.; Veca, E.; Rse, R. Analisi termogravimetrica su campioni di carbone. *Rep. RSE/2009/187* **2009**, 4–12.
32. BS EN 15414-3:2011Solid recovered fuels. Determination of moisture content using the oven dry method. Moisture in general analysis sample.
33. BS 1016-104.4-1998: Methods for analysis and testing of coal and coke. Proximate analysis. Determination of ash.
34. Analisi ambientale della raccolta e del riciclo di prodotti sanitari assorbenti Risultati sintetici. https://www.senato.it/application/xmanager/projects/leg17/attachments/documento_evento_procedura_commissione/files/000/000/636/Documentazione_FATER.pdf
35. Okamoto, H. Supplemental Literature Review of Binary Phase Diagrams: Ag-Nd, Ag-Zr, Al-Nb, B-Re, B-Si, In-Pt, Ir-Y, Na-Si, Na-Zn, Nb-P, Nd-Pt, and Th-Zr. *J. Phase Equilibria Diffus.* **2014**, *35*, 636–648, doi:10.1007/s11669-014-0324-8.
36. Di Giuliano, A.; Lucantonio, S.; Gallucci, K. Devolatilization of Residual Biomasses for Chemical Looping Gasification in Fluidized Beds Made Up of Oxygen-Carriers. *Energies* **2021**, *14*, 311, doi:10.3390/en14020311.
37. Scala, F. Particle agglomeration during fluidized bed combustion: Mechanisms, early detection and possible countermeasures. *Fuel Process. Technol.* 2018.
38. Gibilaro, L.G. *Fluidization - Dynamic*; Butterworth-Heinemann, 2001; ISBN 978-0-7506-5003-8, Imprint https://doi.org/10.1016/B978-0-7506-5003-8.X5000-9.
39. Basu, P. *Combustion and gasification in fluidized beds*; CRC/Taylor & Francis, 2006; ISBN 9780849333965.
40. Don W.Green, R.H.Pe. *Perry Chemical Engineers Handbook*; 2016; Vol. 4; ISBN 0071593136.
41. Namkung, H.; Xu, L.H.; Kim, C.H.; Yuan, X.; Kang, T.J.; Kim, H.T. Effect of mineral components on sintering of ash particles at low temperature fouling conditions. *Fuel Process. Technol.* **2016**, *141*, 82–92, doi:10.1016/j.fuproc.2015.06.004.